Boundary layers in rotating weakly turbulent Rayleigh–Bénard convection

Richard J. A. M. Stevens,[1] Herman J. H. Clercx,[2] and Detlef Lohse[1]
[1]*Department of Science and Technology and J. M. Burgers Center for Fluid Dynamics, University of Twente, P.O. Box 217, 7500 AE Enschede, The Netherlands*
[2]*Department of Applied Mathematics, University of Twente, P.O. Box 217, 7500 AE Enschede, The Netherlands and Department of Physics and J. M. Burgers Centre for Fluid Dynamics, Eindhoven University of Technology, P.O. Box 513, 5600 MB Eindhoven, The Netherlands*

(Received 20 February 2010; accepted 23 June 2010; published online 13 August 2010)

The effect of rotation on the boundary layers (BLs) in a Rayleigh–Bénard system at a relatively low Rayleigh number, i.e., $\mathrm{Ra}=4\times10^7$, is studied for different Pr by direct numerical simulations and the results are compared with laminar BL theory. In this regime, we find a smooth onset of the heat transfer enhancement as function of increasing rotation rate. We study this regime in detail and introduce a model based on the Grossmann–Lohse theory to describe the heat transfer enhancement as function of the rotation rate for this relatively low Ra number regime and weak background rotation $\mathrm{Ro}\gtrsim1$. The smooth onset of heat transfer enhancement observed here is in contrast to the sharp onset observed at larger $\mathrm{Ra}\gtrsim10^8$ by Stevens *et al.* [Phys. Rev. Lett. **103**, 024503 (2009)], although only a small shift in the Ra-Ro-Pr phase space is involved. © *2010 American Institute of Physics*. [doi:10.1063/1.3467900]

I. INTRODUCTION

Normally, the transition between different turbulent states is smooth because the large random fluctuations that characterize the turbulent flow make sure that the entire phase space is explored, and therefore the transitions between different states, which are explored as a control parameter is changed, are washed out. A classical system to study turbulence is Rayleigh–Bénard (RB) convection.[1–3] For given aspect ratio $\Gamma\equiv D/L$ (D is the cell diameter and L is its height) and given geometry, its dynamics are determined by the Rayleigh number $\mathrm{Ra}=\beta g\Delta L^3/(\kappa\nu)$ and the Prandtl number $\mathrm{Pr}=\nu/\kappa$. Here, β is the thermal expansion coefficient, g is the gravitational acceleration, Δ is the temperature difference between the plates, and ν and κ are the kinematic and thermal diffusivity, respectively. The heat transfer in a RB system can satisfactorily be described by the Grossmann–Lohse (GL) theory[1,4–7] and shows that RB convection has different turbulent regimes in the Ra-Pr phase space (see Fig. 3 of Ref. 1). The case where the RB system is rotated around a vertical axis, i.e., rotating Rayleigh–Bénard (RRB) convection, at an angular speed Ω is interesting for industrial applications and problems in geology, oceanography, climatology, and astronomy. The rotation rate of the system is nondimensionalized in the form of the Rossby number $\mathrm{Ro}=\sqrt{\beta g\Delta/L}/(2\Omega)$. The dynamics of RRB convection are thus determined by three control parameters, i.e., Ra, Pr, and Ro, and this leads to a huge Ra-Pr-Ro phase space (see Fig. 1).

It is widely understood[8] that rotation suppresses convective flow, and with it convective heat transport, when the rate of rotation is sufficiently large. However, experimental[9–18] and numerical[16–24] studies on RRB convection have shown that rotation can also enhance the heat transport with respect to the nonrotating case. This heat transport enhancement is caused by Ekman pumping[11,15–18,20,22,24–26] and its efficiency depends strongly on the combination of Ra, Pr, and Ro.[17,18,24] In this paper, we will discuss the results of direct numerical simulations (DNS) that show that this heat transfer enhancement as function of the Ro number is smooth for relatively low Ra number, here $\mathrm{Ra}=4\times10^7$ [see Fig. 2(a)], while experimental and numerical data for $\mathrm{Ra}=2.73\times10^8$ and $\mathrm{Pr}=6.26$ show a sharp onset for the heat transport enhancement [see Fig. 2(b)]. This difference is remarkable since only a small shift in the Ra-Pr-Ro phase space is involved (see Fig. 1).

In this paper, we will first describe the flow characteristics found in the simulations. We will show that there is a smooth transition from one turbulent regime to another for the relatively low Ra number regime whereas a sharp transition is found for higher Ra. In Sec. II, we will discuss the properties of the boundary layers (BLs) found in the DNS in detail. Subsequently, the laminar BL theory for flow over an infinitely large rotating disk will be discussed in Sec. III in order to explain the BL properties found in the DNS. The derived scaling laws from this theory will be used in a model based on the GL theory to describe the heat transfer enhancement as function of Ro for the relatively low Ra number regime with weak background rotation (see Sec. IV).

II. NUMERICAL RESULTS FOR BOUNDARY LAYERS IN RRB CONVECTION

The flow characteristics of RRB convection for $\mathrm{Ra}=4\times10^7$, $1<\mathrm{Ro}<\infty$, $0.2<\mathrm{Pr}<20$, and aspect ratio $\Gamma=1$, are obtained from solving the three-dimensional Navier–Stokes equations within the Boussinesq approximation

$$\frac{D\mathbf{u}}{Dt}=-\nabla P+\left(\frac{\mathrm{Pr}}{\mathrm{Ra}}\right)^{1/2}\nabla^2\mathbf{u}+\theta\hat{z}-\frac{1}{\mathrm{Ro}}\hat{z}\times\mathbf{u}, \tag{1}$$

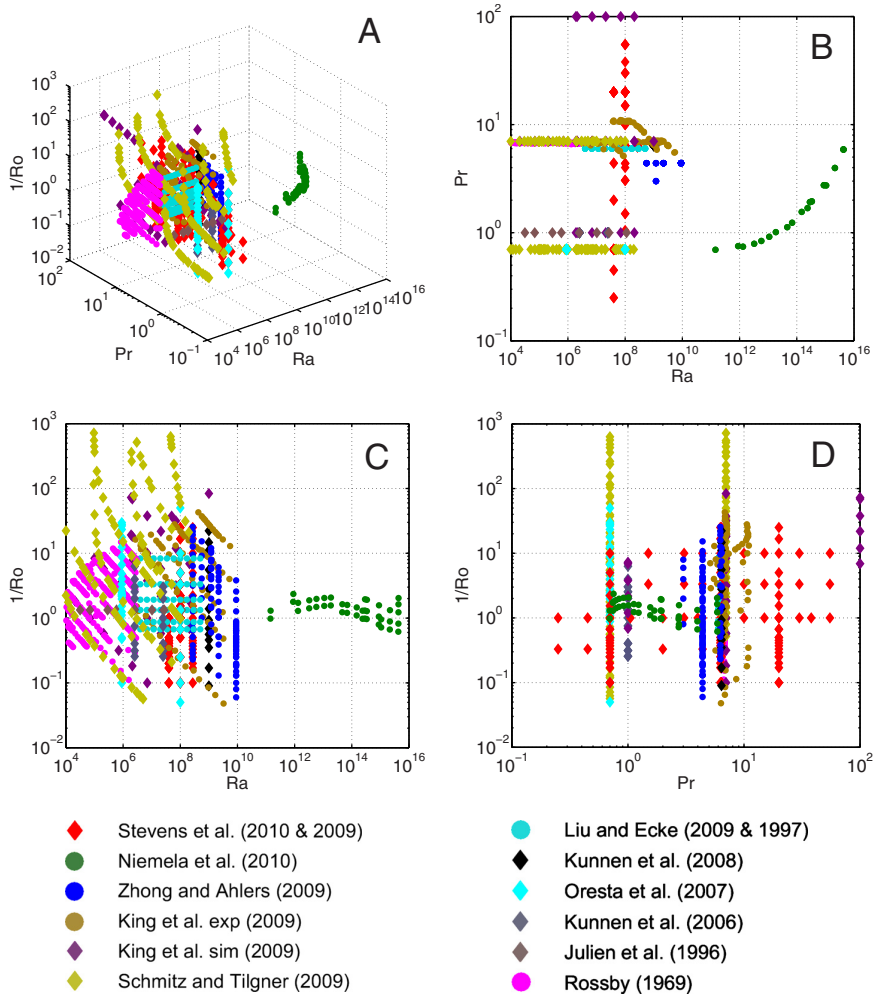

FIG. 1. (Color online) Phase diagram in Ra-Pr-Ro space for RRB convection. The data points indicate where Nu has been measured or numerically calculated. The data are obtained in a cylindrical cell with aspect ratio $\Gamma=1$ with no-slip boundary conditions, unless mentioned otherwise. The data from direct numerical simulations and experiments are indicated by diamonds and dots, respectively. The data sets, which are ordered chronologically in panel (e), are from Stevens *et al.* (Refs. 17, 18, and 24, and the simulations of this study); Niemela *et al.* (Ref. 27) ($\Gamma=0.5$); Zhong and Ahlers (Refs. 17 and 18); King *et al.* (Ref. 16); Schmitz and Tilgner (Ref. 23) (free slip boundary conditions and horizontally periodic); Liu and Ecke (Refs. 9 and 10) (square with $\Gamma=0.78$); Kunnen *et al.* (Ref. 22); Oresta *et al.* (Ref. 19) ($\Gamma=0.5$); Kunnen *et al.* (Ref. 28) ($\Gamma=2$, horizontally periodic); Julien *et al.* (Ref. 20) ($\Gamma=2$, horizontally periodic); and Rossby (varying aspect ratio). Panel (a) shows a three-dimensional view on the phase space (see also the linked movie). (b) Projection on the Ra-Pr phase space. (c) Projection on the Ra-Ro phase space. (d) Projection on the Pr-Ro phase space (enhanced online). [URL: http://dx.doi.org/10.1063/1.3467900.1]

$$\frac{D\theta}{Dt} = \frac{1}{(\mathrm{PrRa})^{1/2}}\nabla^2\theta, \tag{2}$$

with $\nabla\cdot\mathbf{u}=0$. Here, $\hat{z}$ is the unit vector pointing in the opposite direction to gravity, $D/Dt=\partial_t+\mathbf{u}\cdot\nabla$ is the material derivative, $\mathbf{u}$ is the velocity vector (with no-slip boundary conditions at all walls), and θ is the nondimensional temperature $0\leq\theta\leq1$. Finally, P is the reduced pressure (separated from its hydrostatic contribution, but containing the centripetal contributions): $P=p-r^2/(8\mathrm{Ro}^2)$, with r as the distance to the rotation axis. The equations have been made nondimensional by using, next to L and Δ, the free-fall velocity $U=\sqrt{\beta g\Delta L}$. A constant temperature boundary condition is used at the bottom and top plate and the side wall is adiabatic. Further details about the numerical procedure can be found in Refs. 29–31.

The first set of simulations is used to study the Ro number dependence of the following quantities: the normalized heat transfer, the thickness of the thermal BL, and the normalized averaged root mean square (rms) vertical velocity fluctuations. Here we have simulated RRB convection at several Ro numbers for three different Pr numbers (Pr=0.7, Pr=6.4, and Pr=20). All these simulations are performed on a grid with $65\times193\times129$ nodes, respectively, in the radial, azimuthal, and vertical directions, allowing for sufficient resolution in the bulk and the BL according the resolution criteria set in Ref. 32. The Nusselt number is calculated in several ways as is discussed in detail in Ref. 24 and its statistical convergence has been controlled. Some data for Pr=6.4 have already been published in Ref. 18. There, the average was over 4000 dimensionless time units. The new results for Pr=0.7 and Pr=20 are averaged over 2500 dimensionless time units. Note that we simulated the flow for a large number of eddy turnover times to reduce the statistical error in the obtained Nusselt number results and to prevent the influence of transient effects. This is necessary to accurately resolve the transition regime where the heat transfer starts to increase and to accurately determine the flow statistics. Furthermore, we note that all simulations are started from a new flow field in order to rule out hysteresis effects.

The second set of simulations is used to study the Pr number dependence of the same set of quantities. Here we simulated RRB for several Pr numbers and three different Ro numbers (Ro=∞, Ro=3, and Ro=1). The simulations for $\mathrm{Pr}\geqq0.70$ are performed on a $97\times257\times193$ and the simulations at Pr=0.25 and Pr=0.45 are performed on a $129\times385\times257$ grid. The finer resolution is needed here as the

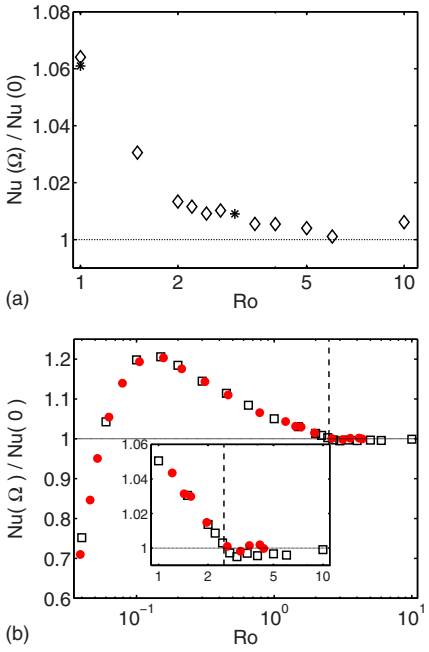

FIG. 2. (Color online) Normalized heat transfer as a function of the Rossby number. (a) Numerical results for $Ra=4\times10^7$ and Pr=6.4. The diamonds and stars indicate the results obtained on the $193\times65\times129$ and $257\times97\times193$ grid, respectively. (b) $Ra=2.73\times10^8$ and Pr=6.26. Solid circles: experimental data (Ref. 18) Open squares: numerical results (Refs. 17 and 18). The vertical dashed line indicates the position of the onset.

structure of the flow changes and the Reynolds number based on the LSC increases for lower Pr. For most cases, the flow is simulated for 400 dimensionless time units and 200 dimensionless time units were simulated before data are collected to prevent any influence of transient effects.[24] For Pr =2 and Pr=4.4, we averaged over 1200 dimensionless time units in order to obtain more accurate statistics on the velocity field. Note that the second set of simulations is partially overlapping with the first set of simulations. We find that results obtained on the different grids are very similar, i.e., the difference is generally between 0.5% and 1% [see Figs. 2(a), 5(a), and 7(a)]. Again, all simulations are started from a new flow field in order to rule out any hysteresis effects.

Figure 3 shows the azimuthally averaged temperature profile at the cylinder axis for different system parameters. In previous numerical studies concerning (rotating) RB convection, the thermal BL thickness is usually defined by either looking at the maximum rms value of the temperature fluctuations or by considering the BL thickness based on the slope of the mean temperature profile. In the latter case, it is usually assumed that no mean temperature gradient exists in the bulk (the BL thickness according to this assumption is denoted by λ_θ^{sl-ng}). The temperature gradient in the bulk is, however, strongly influenced by rotation[17,33] and, when rotation is present, also by Pr (see Fig. 4). We define the thermal BL thickness λ_θ^{sl} as the intersection point between the linear extrapolation of the temperature gradient at the plate with the linear fit to the temperature profile in the bulk region $(0.25L<z<0.75L)$ [see Fig. 3(a)]. From now on, this definition of the thermal BL thickness will be used.

For the relatively low Ra number regime, here $Ra=4\times10^7$, the heat transfer enhancement as function of Ro is smooth [see Fig. 5(a)]. Note that although the behavior of λ_θ^{sl} [see Fig. 5(b)], i.e., the horizontally averaged value of the radially dependent thermal BL thickness $[\lambda_\theta^{sl}(r)]$, as function of Ro is similar for all Pr the behavior of Nu is very different. This is due to the influence of Pr on the effect of Ekman pumping.[17,24] At low Pr, the larger thermal diffusivity limits the effect of Ekman pumping and causes a larger destabilizing temperature gradient in the bulk[17,24] (see Fig. 4). Due to the limited effect of Ekman pumping, there is no heat transport enhancement for low Pr (see Fig. 5).

Figure 6 shows that the volume averaged $\mathrm{Re}_{z,\mathrm{rms}}$ (dimensionless rms velocity of the axial velocity fluctuations), which is a measure for the strength of the LSC, decreases strongly for strong enough rotation. The vertical dashed lines in Fig. 6 indicate the position where $\mathrm{Re}_{z,\mathrm{rms}}(\Omega)/\mathrm{Re}_{z,\mathrm{rms}}(0)$ becomes smaller than 1, which we use to indicate the point at which the LSC strength starts to decrease. This value is determined by extrapolating the behavior observed at low Ro numbers to reduce the effect of the uncertainty in single data points. In Ref. 18 (see Fig. 3 of that paper), we also used this method to indicate the position of the onset of the heat transfer enhancement in the high Ra number regime. However, for this lower Ra number, we do not find any evidence for a sudden onset around this point (see Fig. 5), where the vertical lines are plotted at the same positions as in Fig. 6. In contrast to the decrease in the volume averaged value of $\mathrm{Re}_{z,\mathrm{rms}}$, the horizontally averaged value of $\mathrm{Re}_{z,\mathrm{rms}}$ at the edge of the thermal BL (thus at the distance $\lambda_\theta^{sl}(r)$ from either the top or bottom boundary) increases. This indicates that Ekman pumping, which is responsible for the increase in Nu, sets in and no sign of Ekman pumping prior to the decrease in LSC strength is found. Figure 6 thus shows that the flow makes a transition between two different turbulent states, i.e., a transition from a LSC dominated regime to an Ekman pumping dominated regime.[18] Figure 6(a) shows no increase in the horizontally averaged value of $\mathrm{Re}_{z,\mathrm{rms}}$ at the edge of the thermal BL for Pr=0.7 because the flow is suppressed for higher Ro, i.e., lower rotation rate, when Pr is lower (see the discussion in Ref. 24).

The Pr number dependence of the Nu number and the thickness of the thermal BL is shown in Fig. 7. From Fig. 7(a), we can conclude that hardly any Pr number dependence on the Nu number exists in the weak rotating regime (Ro =3). However, a strong Pr number effect appears for stronger rotation rates, where Ekman pumping is the dominant effect.[17] Figure 7(b) shows that the effect of weak background rotation on the thermal BL thickness is largest for $\mathrm{Pr}\approx2$. The Pr number dependence of $\mathrm{Re}_{z,\mathrm{rms}}$ is shown in Fig. 8. The difference between the data points obtained for the bottom and top BL in Fig. 8 indicate the uncertainty in the results. Increasing the averaging time, which we checked for Pr=2 and Pr=4.4, reduces the differences for the data points obtained for the bottom and top BL. Furthermore, we note that it is important to take the radial thermal BL dependence $[\lambda_\theta^{sl}(r)]$ into account for lower Pr, where the radial BL dependence is strongest, and we excluded the region close to

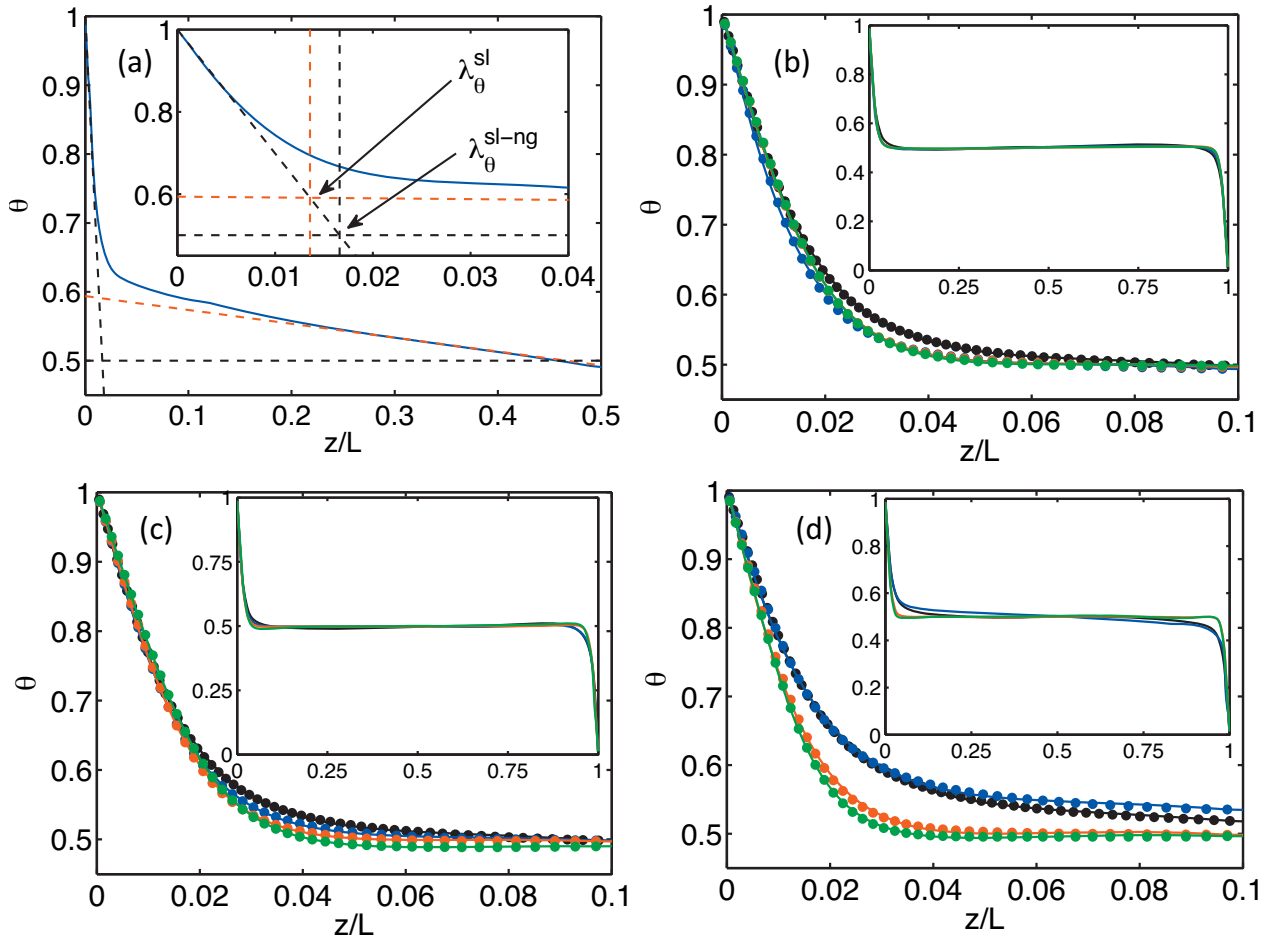

FIG. 3. (Color) (a) Visualization of the definitions of the thermal BL thicknesses λ_θ^{sl} and λ_θ^{sl-ng} (assuming zero gradient in the bulk). [(b)–(d)] Azimuthally averaged temperature profiles for $Ra=4\times10^7$ and different Pr and Ro numbers at the cylinder axis $r=0$ for (b) $Ro=\infty$, (c) Ro=3, and (d) Ro=1. Black, blue, red, and dark green indicate the profiles for Pr=0.25, Pr=0.7, Pr=6.4, and Pr=20, respectively. The dots indicate the data points obtained from the simulations. The insets show the profile over the full cell.

the sidewall ($0.45L \le r \le 0.5L$) from the horizontal averaging in order to eliminate the effect of the sidewall.

The computation of the kinetic BL thickness can be either based on the position of the maximum rms value of the azimuthal velocity fluctuations[18,34] or on the position of the maximum value of $\epsilon_u'' := \mathbf{u}\cdot\nabla^2\mathbf{u}$, i.e., two times the height at which this quantity is highest, as shown in Ref. 24. In Ref. 35, we compare the result of this empirical method with theoretical results and show that it is indeed a suitable method to define the kinetic BL thickness. Here we first average ϵ_u'' horizontally in the range $0.05L \le r \le 0.45L$ before we determine the position of the maximum. This r range has been taken to exclude the region close to the sidewall, where ϵ_u'' misrepresents the kinetic BL thickness due to the rising plumes, and the region close to the cylinder axis, since there it is numerically very difficult to reliably calculate ϵ_u'', due to the singularity in the coordinate system. When the radially dependent kinetic BL thickness $[\lambda_u^{\epsilon_u''}(r)]$ is horizontally averaged, a small difference, depending on the averaging time, is observed between the bottom and top because of the specific orientation of the LSC. We note that the same quantity ϵ_u'' is used in Ref. 24, where it is shown that the kinetic BL thickness based on ϵ_u'' represents the BL thickness better than the one considering the maximum rms velocity fluctuations, which is normally used in the literature. The volume averaged value of ϵ_u'' is the same as the volume averaged kinetic energy dissipation rate ϵ_u (although it differs locally), which can easily be derived using Gauss's theorem.[1] Figure 9 shows the azimuthally averaged profiles for $\epsilon_u''(\mathrm{RaPr})^{1/2}$ at $r=0.25L$. The normalization factor $(\mathrm{RaPr})^{1/2}$ is used to get Nu number values for all profiles (see Ref. 31). In Fig. 10, the kinetic BL thickness based on the position of the maximum kinetic dissipation rate is shown as function of Ro and Pr. To compare the relative changes in the kinetic BL thicknesses, the values are normalized by values for the nonrotating case. For all Pr numbers, there is a change in the BL behavior at the point where the LSC decreases in strength [vertical dashed lines in Fig. 10(a)]. We see no clear change in the thickness of the kinetic BL thickness before the onset. This could be caused by the method we use to define the kinetic BL thickness, i.e., the data close to the sidewall and the cylinder axis were excluded since the method based on the

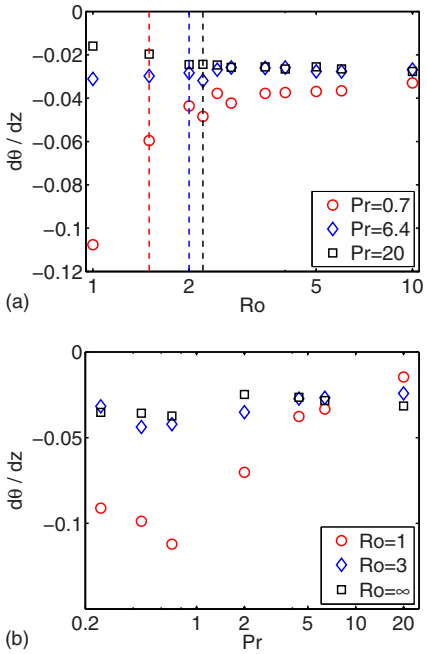

FIG. 4. (Color online) (a) Horizontally averaged temperature gradient at midheight as a function of Ro for $Ra=4\times10^7$ and different Pr. The circles, diamonds, and squares indicate the data for Pr=0.7, Pr=6.4, and Pr=20, respectively. (b) Temperature gradient at midheight as function of Pr for $Ra=4\times10^7$ and different Ro. The circles, diamonds, and squares are the data for Ro=1, Ro=3, and Ro=∞, respectively. The vertical dashed lines (from left to right for Pr=0.7, Pr=6.4, and Pr=20) in (a) indicate the position of the onset (see Fig. 6).

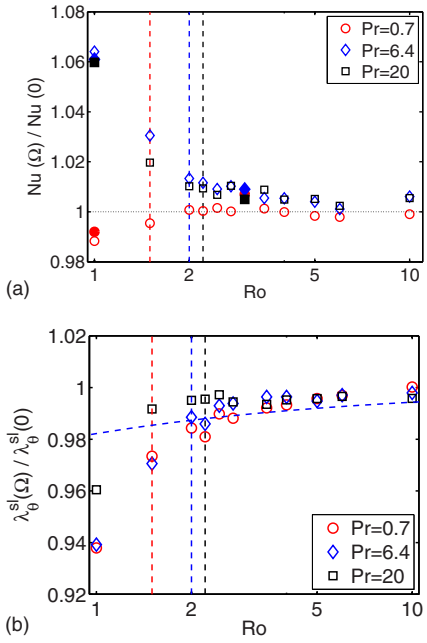

FIG. 5. (Color online) (a) Normalized heat transfer as a function of Ro for $Ra=4\times10^7$ and different Pr. The circles, diamonds, and squares are the data for Pr=0.7, Pr=6.4, and Pr=20, respectively. The dashed-dotted line is the fit obtained by the model equation (22), with $\alpha=55$. The filled symbols indicate the results from the grid refinement check (see text). (b) Horizontally averaged thickness of the thermal BL λ_θ^{sl} as function of Ro. Symbols as in (a) and the dashed-dotted line indicates the same model fit as in (a). The vertical dashed lines (from left to right for Pr=0.7, Pr=6.4, and Pr=20) in both graphs represent the point at which the LSC strength starts to decrease (see Fig. 6).

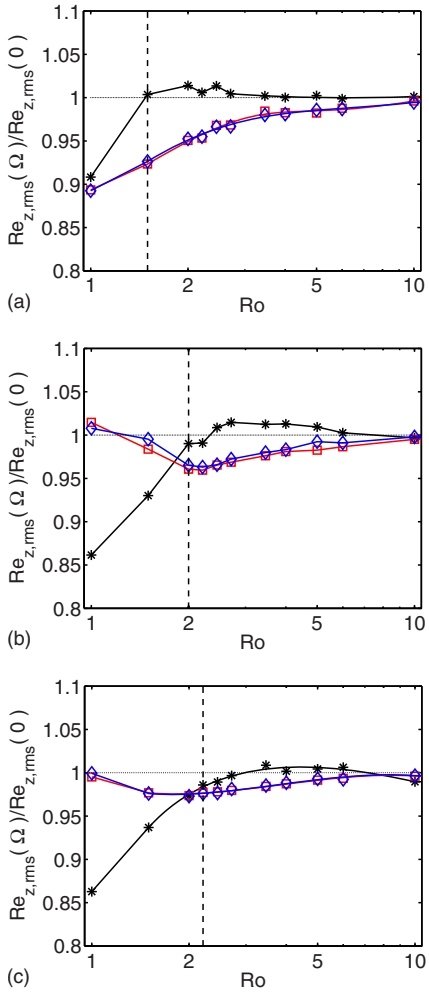

FIG. 6. (Color online) The normalized averaged rms vertical velocity fluctuations $Re_{z,rms}$ for $Ra=4\times10^7$ and different Pr as function of Ro. The stars indicate the volume averaged value of $Re_{z,rms}$. The squares and diamonds indicate the horizontally averaged values of the $Re_{z,rms}$ at a distance $\lambda_\theta^{sl}(r)$ from the lower and upper plate, respectively. The vertical dashed lines again indicate the position where the LSC strength starts to decrease. (a) Pr=0.7, (b) Pr=6.4, and (c) Pr=20.

maximum position of ϵ_u'' misrepresents the kinetic BL thickness in these regions.

Figure 10(c) shows that when the kinetic BL thickness is based on the position of the maximum value of ϵ_u'' its thickness increases with $Pr^{1/3}$, which is in agreement with the GL model. Namely, since $\lambda_u=aH/\sqrt{Re}$ and the simulations are mostly in regime II_u, where $Re\sim Pr^{-2/3}$, this gives a scaling of $Pr^{1/3}$ scaling for the kinetic BL thickness. In nonrotating measurements in a cylindrical geometry, Lam *et al.*[36] used the position of the maximum velocity to determine the kinetic BL thickness and they found the exponent to be 0.24 over a wide range of Pr. When we base the kinetic BL thickness on the position of the maximum rms velocity fluctuations, which is closely related to the position of the maximum velocity, we get an exponent of 0.21 [see Fig. 10(c)]. This is in excellent agreement with the experimental measurements, since the higher Pr numbers used in the experi-

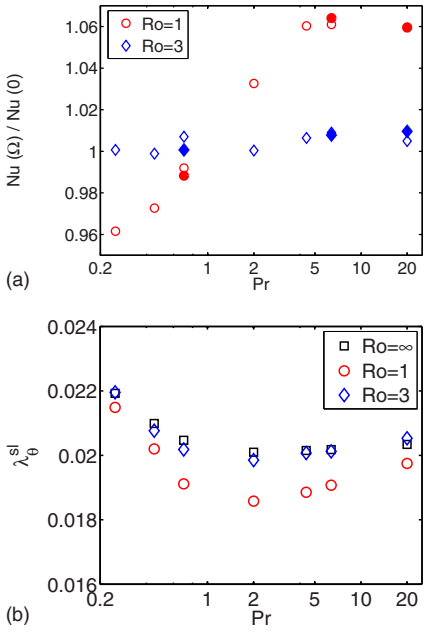

FIG. 7. (Color online) (a) Normalized heat transfer as a function of Pr number for $Ra=4\times10^7$ and different Ro. The circles and diamonds indicate the data for Ro=1 and Ro=3, respectively. The open and filled symbols indicate the results obtained on the $97\times257\times193$ and the $65\times193\times129$ grid, respectively. (b) Horizontally averaged thermal BL thickness λ_θ^{sl} as function of Pr. Symbols as in (a) and squares for Ro=∞.

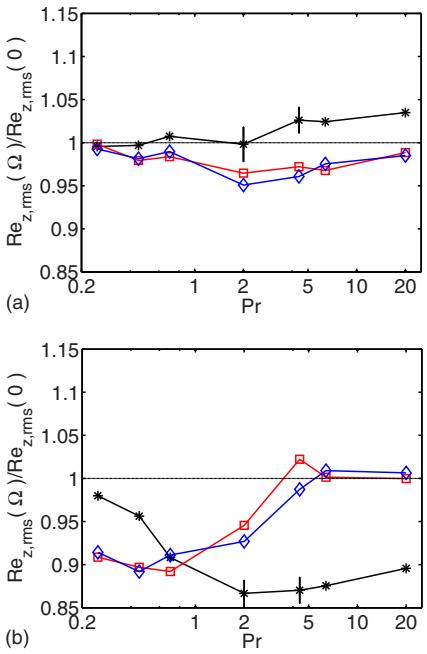

FIG. 8. (Color online) The normalized averaged rms vertical velocity fluctuations $Re_{z,rms}$ for $Ra=4\times10^7$ and different Ro as function of Pr. The stars indicate the volume averaged value of $Re_{z,rms}$. The vertical error bars at Pr =2 and Pr=4.4 indicate the difference in the volume averaged value obtained after 1200 dimensionless time units (data point) and 400 dimensionless time units. The squares and the diamonds indicate the horizontally averaged $Re_{z,rms}$ at a distance $\lambda_\theta^{sl}(r)$ from the lower and upper plate, respectively. (a) Ro=3 and (b) Ro=1.

ments go more toward regimes I_u and IV_u of the GL theory than the numerical data and in these regimes, a slightly higher exponent is expected.

We conclude this section with a brief summary of the results obtained for the high Ra number regime.[17,18] For $Ra\gtrsim1\times10^8$ a sudden onset at $Ro=Ro_c$ in the heat transport enhancement occurs [see Fig. 2(b)], where we find a smooth transition at lower Ra [see Fig. 2(a)]. Figure 11(a) shows the volume averaged ratio $Re_{z,rms}(\Omega)/Re_{z,rms}(0)$. The behavior is similar to the one observed at lower Ra (see Fig. 6). For the high Ra number regime, the onset at Ro_c is defined as the point where the ratio $Re_{z,rms}(\Omega)/Re_{z,rms}(0)$ becomes smaller than 1. For the low Ra number, this point indicates the position where the LSC strength starts to decrease and just as for the relatively low Ra number regime, Ekman pumping in the high Ra number regime is indicated by an increase of the horizontally averaged $Re_{z,rms}$ value at the edge of the thermal BL. Although the two cases, i.e., the relatively low Ra number regime and the high Ra number regime both show a transition between two different turbulent states, the important difference between the two is that the transition is sharp in the high Ra number regime and smooth in the relatively low Ra number regime. The onset in the high Ra number regime is also observed in the behavior of the BLs. Figure 11(b) shows that the kinetic BL thickness does not change below onset ($Ro>Ro_c$) and above onset, the BL behavior is dominated by rotational effects and thus Ekman scaling (proportional to $Ro^{1/2}$) is observed. This scaling factor is also found in the laminar BL theory, which will be discussed in Sec. III. Finally, Fig. 11(c) shows the thermal BL thickness λ_θ^{sl}.

III. BOUNDARY LAYER THEORY FOR WEAK BACKGROUND ROTATION

In Sec. II, we observed that there is a smooth increase in the heat transfer as function of the Ro number when the Ra number is relatively low. In this section, we set out to account for the increase in the heat transfer as function of the rotation rate within a model, which extends the ideas of the GL theory to the rotating case. In the GL theory, the Prandtl–Blasius BL theory for laminar flow over an infinitely large plate was employed in order to estimate the thicknesses of the kinetic and thermal BLs and the kinetic and thermal dissipation rates. These results were then connected with the Ra and Pr number dependence of the Nusselt number. In perfect analogy, in the present paper we apply laminar BL theory for the flow over an infinitely large rotating plate to study the effect of rotation on the scaling laws. We stress that employing the results of laminar BL theory over an infinite rotating disk to the rotating RB case in a closed cylinder is fully analogous to employing Prandtl–Blasius BL theory for flow over an infinite plate to the standard RB case without rotation, where the method was very successful.[1,4–7]

In both cases, the equations used to derive the scaling laws are time independent and therefore the resulting solutions are associated with laminar flow. However, evidently, high Rayleigh number thermal convection is time-dependent. Therefore one wonders whether the derived scaling laws still

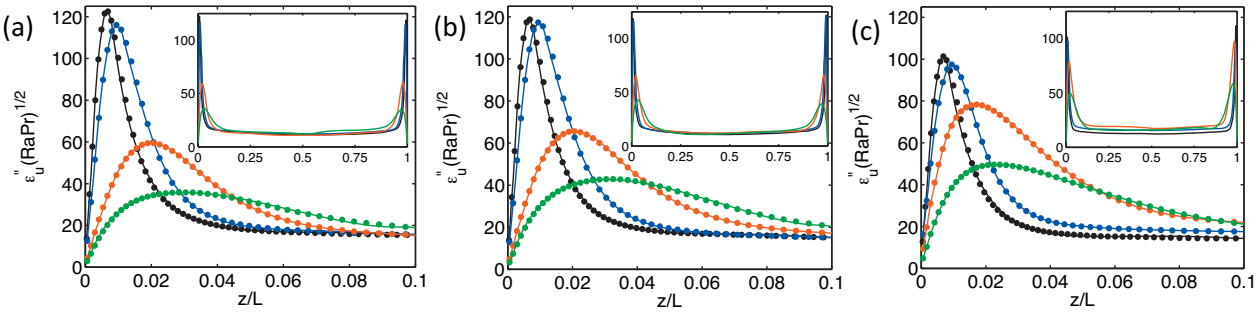

FIG. 9. (Color) Azimuthally averaged profile of $\epsilon_u''(\mathrm{RaPr})^{1/2}$ for $\mathrm{Ra}=4\times10^7$ and different Pr and Ro at the radial position $r=0.25L$. The figures, from left to right, are for Ro=∞, Ro=3, and Ro=1. Black, blue, red, and green indicate the profiles for Pr=0.25, Pr=0.7, Pr=6.4, and Pr=20, respectively. The dots indicate the data points obtained from the simulations. The insets shows the profile over the whole domain.

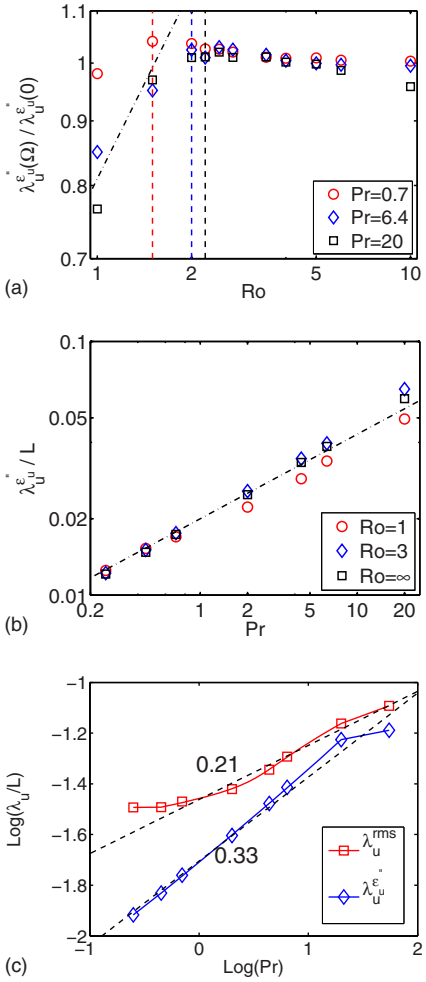

FIG. 10. (Color online) (a) The thickness of the kinetic BL and the average of bottom and top BL, based on the position of the maximum value of ϵ_u'' for $\mathrm{Ra}=4\times10^7$ and different Pr. The circles, diamonds, and squares are the data for Pr=0.7, Pr=6.4, and Pr=20, respectively. The dashed-dotted line indicates $\mathrm{Ro}^{1/2}$ scaling. The vertical dashed lines (from left to right for Pr=0.7, Pr=6.4, and Pr=20) represent the point at which the LSC strength starts to decrease. (b) As in (a), but now for different Ro. The circles, diamonds, and squares are the data for Ro=1, Ro=3, and Ro=∞, respectively. The dashed-dotted line indicates $\mathrm{Pr}^{1/3}$ scaling. (c) The kinetic BL thickness based on the position of the maximum value of ϵ_u'' and based on the position of the maximum rms velocity fluctuations are indicated by diamonds and squares, respectively.

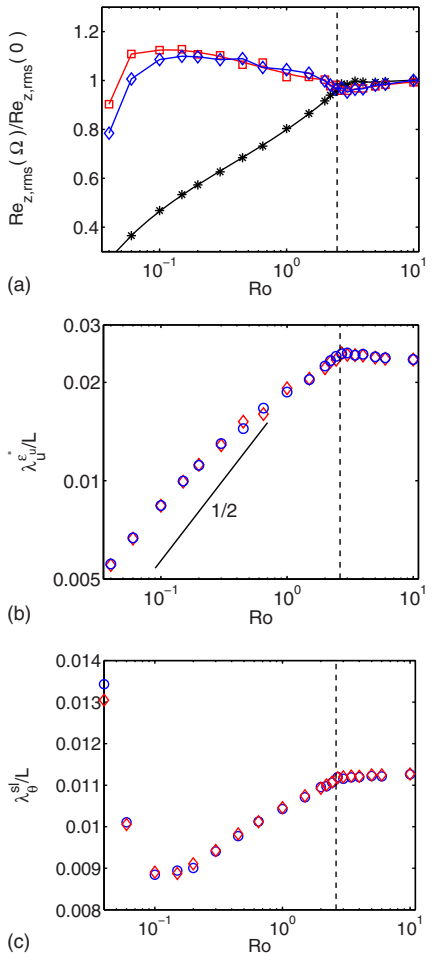

FIG. 11. (Color online) (a) The averaged rms vertical velocities $\mathrm{Re}_{z,\mathrm{rms}}$ as function of Ro. The stars indicate the volume averaged value of $\mathrm{Re}_{z,\mathrm{rms}}$. The squares and diamonds, respectively, indicate the horizontally averaged $\mathrm{Re}_{z,\mathrm{rms}}$ at the distance $\lambda_\theta^{sl}(r)$ from the bottom and top plate. (b) The thickness of the kinetic top and bottom BLs based on the position of the maximum ϵ_u'': diamonds (circles) for top (bottom) BL. The vertical dashed lines in panels (a) and (b) indicate the position of Ro_c. Here, the BL behavior changes from Prandtl–Blasius (right) to Ekman (left) (Ref. 18). (c) The circles (diamonds) indicate λ_θ^{sl} for the bottom (top) plate.

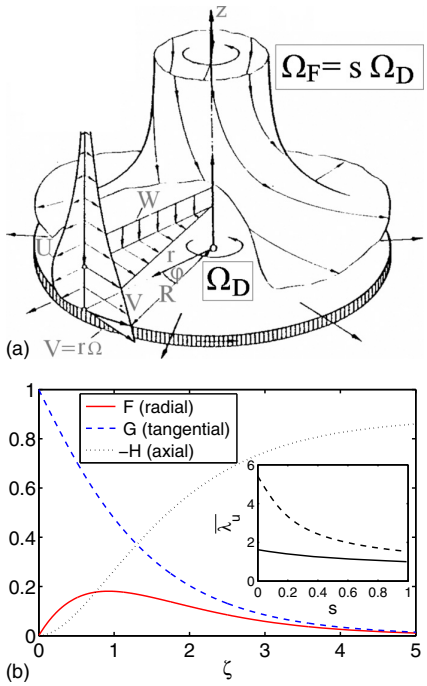

FIG. 12. (Color online) (a) Flow near a disk rotating with an angular velocity Ω_D when the fluid at infinity is rotating with $\Omega_F = s\Omega_D$. Adapted from Ref. 39. (b) Velocity components in the von Kármán case. The inset shows $\bar{\lambda}_u^{sl}$ (solid line) and $\bar{\lambda}_u^{99\%}$ (dashed line).

hold for time-dependent flow over an infinite rotating disk. We will show that the Ro and Pr scaling that is derived is not changed when temporal changes are included. This is again in perfect analogy to the Prandtl–Blasius BL case where the scaling laws also hold for time-dependent flow provided that the viscous BL does not break down.[7] Indeed, recent experiments and numerical simulations[37,38] have shown that in nonrotating RB, the BLs scaling wise behave as in laminar flow and therefore we feel confident to assume the same for the weakly rotating case. The basic idea of the model we introduce is to combine the effect of the LSC roll, which is implemented in the GL theory by the use of laminar Prandtl–Blasius BL theory over an infinitely large plate, and the influence of the rotation on the thermal BL.

The system we are analyzing to study the influence of rotation on the thermal BL thickness above a heated plate is schematically shown in Fig. 12(a). It is the laminar flow of fluid over an infinite rotating disk. The disk rotates with an angular velocity Ω_D and the fluid at infinity with angular velocity $\Omega_F = s\Omega_D$, with $s < 1$. Figure 12(b) shows that a positive radial velocity is created due to the action of the centrifugal force. Because of continuity, there is a negative axial velocity, i.e., fluid is flowing toward the disk. The system has been analyzed before in the literature, e.g., Refs. 39–43. Here we will briefly summarize the procedure.

The system is analyzed by using the Navier–Stokes equations in cylindrical coordinates and assuming a steady stationary, axial symmetric solution. To reduce the Navier–Stokes equations to a set of ordinary differential equations (ODE), we employ self-similarity. The first step is to determine the dimensionless height in the system just as in the Prandtl–Blasius approach, in which the BL thickness scales as[44] $\delta \sim \sqrt{\nu x/U}$. For the case of a large rotating disk in a fluid rotating around an axis perpendicular to the disk, the thickness of the BL can be estimated by replacing U by $\Omega_D x$.[44] The thickness then scales as $\delta \sim \sqrt{\nu/\Omega_D}$. The similarity variable in the system is the dimensionless height

$$\zeta = z\sqrt{\frac{\Omega_D}{\nu}}. \tag{3}$$

According to von Kármán, the following self-similarity Ansatz for the velocity components and the pressure can be taken:[39–43]

$$u = r\Omega_D F(\zeta), \tag{4}$$

$$v = r\Omega_D G(\zeta), \tag{5}$$

$$w = \sqrt{\nu\Omega_D} H(\zeta), \tag{6}$$

$$p = \rho\nu\Omega_D P(\zeta) + \tfrac{1}{2}\rho s^2 \Omega_D^2 r^2. \tag{7}$$

After substitution into the Navier–Stokes equations, one obtains a system of four coupled ODEs,

$$F^2 + F'H - G^2 - F'' + s^2 = 0, \tag{8}$$

$$2FG + HG' - G'' = 0, \tag{9}$$

$$P' + HH' - H'' = 0, \tag{10}$$

$$2F + H' = 0, \tag{11}$$

where the prime indicates differentiation with respect to ζ. This set of ODEs must be supplemented by the boundary conditions

$$u = 0, \quad v = r\Omega_D, \quad w = 0 \quad \text{for } z = 0, \tag{12}$$

$$u = 0, \quad v = sr\Omega_D \quad \text{for } z = \infty. \tag{13}$$

When substituting the self-similarity Ansätze (4)–(7) into these boundary conditions, one obtains

$$F = 0, \quad G = 1, \quad H = 0 \quad \text{for } \zeta = 0, \tag{14}$$

$$F = 0, \quad G = s \quad \text{for } \zeta = \infty. \tag{15}$$

Note that the boundary condition at infinity together with the continuity equation (11) gives $H'(\zeta \to \infty) = 0$. One can further simplify the set of ODEs by realizing that the ODE for the pressure (10) is decoupled from the ODEs determining the velocity profiles by using the continuity equation (11) in Eq. (10) and subsequently integrating this relation. The velocity profiles for the von Kármán case ($s = 0$) are shown in Fig. 12(b). The inset shows that the dimensionless kinetic BL thickness $\bar{\lambda}_u \equiv \lambda_u/\delta$ decreases with increasing relative rotation rate s of the fluid at infinity. This is due to the decreasing effect of the centrifugal force. We determined $\bar{\lambda}_u^{99\%}$, the dimensionless kinetic BL thickness at which the velocity has achieved 99% of the outer flow velocity, using the tangential velocity profile, i.e., when $G(\zeta) = s + 0.01(1-s)$. Additionally,

we calculated $\bar{\lambda}_u^{sl}$, the dimensionless kinetic BL thickness based on the slope of the tangential velocity at the disk. The scaling of the kinetic BL predicted by the above rotating BL theory, i.e., $\mathrm{Ro}^{1/2}$, is the classical Ekman scaling. In the simulations of RRB, we find the same scaling of the kinetic BL once the flow is dominated by rotational effect, i.e., $\mathrm{Ro} \lesssim \mathrm{Ro}_c$ [see Fig. 11(b)].

The GL theory heavily builds on laminar Prandtl–Blasius BL theory, which describes the laminar flow over an infinite plate. In the Prandtl–Blasius theory, the temperature field is assumed to be passive to derive the Pr number scaling. As we want to extend the GL theory to the rotating case we keep this analysis analogous to the Prandtl–Blasius theory. Therefore, we assume the temperature field to be passive in order to derive the scaling laws as function of the Pr number. We nondimensionalize the temperature by

$$\tilde{\theta}(\zeta) = \frac{\theta - \theta_\infty}{\theta_b - \theta_\infty}, \tag{16}$$

where θ_b is the temperature of the bottom disk and $\theta_\infty < \theta_b$ is the ambient temperature. Then, one obtains the following ODE describing the temperature field:[45–47]

$$\tilde{\theta}' = \mathrm{Pr} H(\zeta) \tilde{\theta}', \tag{17}$$

where the prime indicates a differentiation with respect to ζ. The boundary conditions are

$$\tilde{\theta} = 1 \quad \text{for} \quad \zeta = 0, \tag{18}$$

$$\tilde{\theta} = 0 \quad \text{for} \quad \zeta = \infty. \tag{19}$$

The resulting system of ODEs subjected to the boundary conditions is solved numerically with a fourth order Runge–Kutta method using a Newton–Raphson root finding method to find the initial conditions. One can take the analytic solution for the Ekman case ($s \approx 1$) (see the Appendix) or the known solution for the Bödewadt case (see, for example, Refs. 39 and 41) as one of the starting cases to determine the solutions over the whole parameter range in s and Pr.

In this way, we obtain the full temperature profile for all s and Pr. For the heat transfer, the most relevant quantity is the thermal BL thickness λ_θ, which we nondimensionalized by δ, thus $\bar{\lambda}_\theta \equiv \lambda_\theta / \delta$. One can distinguish between $\bar{\lambda}_\theta^{sl}$ and $\bar{\lambda}_\theta^{99\%}$, the dimensionless BL thickness based on the 99% criterion, thus when $\tilde{\theta}(\zeta) = 0.01$. Figure 13(a) shows that the asymptotic scaling of $\bar{\lambda}_\theta^{99\%}$ and $\bar{\lambda}_\theta^{sl}$ is the same. Furthermore, the figure shows that rotation does not influence the scaling of the thermal BL thickness in the high Pr regime, because the same scaling, namely, proportional to $\mathrm{Pr}^{-1/3}$, is found as for the Prandtl-Blasius case. However, the rotation does influence the scaling in the low Pr regime, where now $\bar{\lambda}_\theta \propto \mathrm{Pr}^{-1}$ instead of $\bar{\lambda}_\theta \propto \mathrm{Pr}^{-1/2}$ as found in the Prandtl–Blasius case. Notice that $\bar{\lambda}_\theta^{99\%} > \bar{\lambda}_\theta^{sl}$, which is due to the decreasing temperature gradient with increasing height. Note that the thermal BL thickness as given in Fig. 13(a) does not directly represent the heat transfer in rotating RB convection. For weakly rotating RB convection, one should account for the

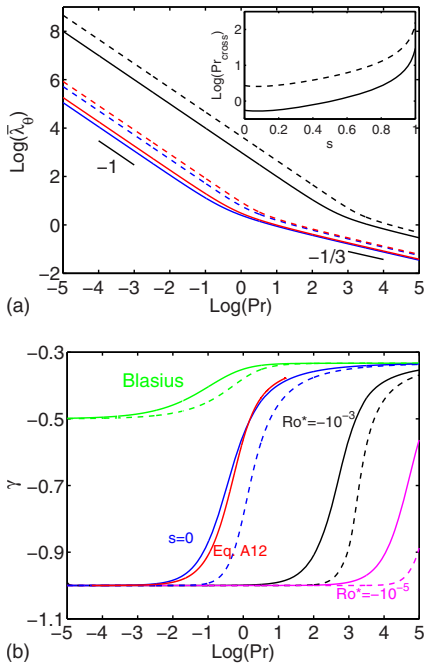

FIG. 13. (Color online) (a) The thermal BL thickness $\bar{\lambda}_\theta \equiv \lambda_\theta / \delta$ as function of Pr. The solid lines from bottom to top indicate $\bar{\lambda}_\theta^{sl}$ for the von Kármán case ($s=0$) for $s=0.5$ and for the Ekman case [$s \approx 1$, $\mathrm{Ro}^* = 10^{-3}$, see definition (A2)], respectively. The dashed lines from bottom to top indicate $\bar{\lambda}_\theta^{99\%}$ for $s=0$, $s=0.5$, and $s \approx 1$, $\mathrm{Ro}^* = 10^{-3}$, respectively. Note that the scaling for the thermal BL thickness goes asymptotically to $\mathrm{Pr}^{-1/3}$ in the high Pr regime and to Pr^{-1} in the low Pr regime. The inset shows $\mathrm{Pr}_{\mathrm{cross}}$, the transition between the high and the low Pr regime as a function of s based on the behavior $\bar{\lambda}_\theta^{sl}$ (solid line) and $\lambda_\theta^{99\%}$ (dashed line). Note that the low Pr regime is more favored for higher s. (b) The solid lines indicate the effective scaling γ in $\bar{\lambda}_\theta \sim \mathrm{Pr}^\gamma$ as function of Pr for $\bar{\lambda}_\theta^{sl}$ for the Blasius case (no rotation), the von Karman case ($s=0$), and the Ekman case ($s \approx 1$) for two Rossby numbers. The corresponding dashed lines indicate the effective scaling for $\bar{\lambda}_\theta^{99\%}$. Also, the analytic prediction [see Eq. (A12)] for the von Kármán case is indicated in the figure.

effect of the LSC, which we will discuss in detail in Sec. IV. And for strongly rotating RB convection, the relation $\mathrm{Nu} = L/(2\lambda_\theta)$ no longer holds, as part of the mean temperature drop is across the bulk (see Fig. 4). This temperature gradient in the bulk is affected by the leaking of plumes out of the Ekman vortices.[17]

In Fig. 13(b), we show the effective power-law exponent $\gamma = (d \log \bar{\lambda}_\theta)/(d \log \mathrm{Pr})$ of an assumed effective power law $\bar{\lambda}_\theta \sim \mathrm{Pr}^\gamma$. It confirms that the effective scaling in the high Pr regime is the same for the Prandtl–Blasius (no rotation) and the von Kármán case ($s=0$), but already at $\mathrm{Pr}=1$, a significant difference is observed.

The temperature advection equation (17) directly suggests the following relation between the scaling of the thermal BL thickness $\bar{\lambda}_\theta^{sl}$ and the scaling of the axial velocity at the edge of the thermal BL $H_{\mathrm{BL}} \sim 1/\mathrm{Pr}\bar{\lambda}_\theta^{sl}$. This immediately implies for the low Pr regime, with $\bar{\lambda}_\theta^{sl} \sim \mathrm{Pr}^{-1}$, that H_{BL} is independent of Pr. For the high Pr regime, with $\bar{\lambda}_\theta^{sl} \sim \mathrm{Pr}^{-1/3}$, it gives $H_{\mathrm{BL}}(\mathrm{Pr}) \sim \mathrm{Pr}^{-2/3}$. The scaling of the thermal BL thickness in the low Pr regime can be understood on physical

grounds. In this regime, $\bar{\lambda}_\theta \gg \bar{\lambda}_u$ and the kinetic BL is fully submerged in the thermal BL. The axial velocity at the edge of the kinetic BL equation (15) is $H_{\mathrm{BL}}=H(\zeta\to\infty)$, as can be shown by applying mass conservation expressed by Eq. (11). As a consequence, in the low Pr regime, the axial velocity is constant in almost the whole thermal BL. Then Eq. (17) can trivially be integrated and immediately gives $\bar{\lambda}_\theta^{sl}\sim \mathrm{Pr}^{-1}$. This derivation is valid for all s, i.e., the scaling in the low Pr regime does not depend on the rotation of the fluid at infinity. The scaling in the high Pr regime is also independent of the rotation of the fluid at infinity. In the Ekman case $s\approx 1$ (see the Appendix), this 1/3 scaling regime shifts toward very large Pr.

Equations (8)–(11) are time independent and therefore the resulting solutions are understood to describe laminar flow. Temporal changes can easily be included by adding $\partial_{\tilde{t}}\tilde{u}_\theta$, $\partial_{\tilde{t}}\tilde{u}_r$, and $\partial_{\tilde{t}}\tilde{u}_z$, where $\tilde{t}=t\Omega_D$ without changing the Ro and Pr scaling discussed above, i.e., the derived scaling laws above still hold for time-dependent flow provided that the viscous BL does not break down. This is in perfect analogy to the Prandtl–Blasius BL case where the scaling laws also hold for time-dependent flow.[7] Recently, Zhou and Xia[38] have developed a method of expressing velocity profiles in the time-dependent BL frame and found that the rescaled profiles agree perfectly with the theoretical Prandtl–Blasius profile. This method could possibly reveal the effect of weak rotation on the BL profiles. However, since the LSC orientation is not known *a priori* in three-dimensional RB convection, it is impossible to sample the BL statistics at the position of the LSC without slightly tilting the sample. Since only very small differences between the BL statistics for nonrotating and weakly rotating RB ($\mathrm{Ro}\gtrsim 2$) are observed, the effect of tilting could significantly influence this comparison. Therefore, such an analysis is beyond the scope of this paper.

To investigate the crossover between the high and the low Pr regime, we define $\mathrm{Pr}_{\mathrm{cross}}$ as the crossover point. $\mathrm{Pr}_{\mathrm{cross}}$ is calculated by determining the intersection between the asymptotic behavior of the high and the low Pr regime. To calculate $\mathrm{Pr}_{\mathrm{cross}}$, we considered $\bar{\lambda}_\theta^{sl}(\mathrm{Pr})$ and $\bar{\lambda}_\theta^{99\%}(\mathrm{Pr})$. The inset of Fig. 13(a) shows that the low Pr regime becomes more favored when the rotation of the fluid at infinity becomes stronger. Then the kinetic BL thickness becomes thinner and the axial velocity decreases, i.e., the thermal BL thickness increases. Because the thermal BL thickness decreases with increasing Pr, the crossover shifts toward higher Pr as is shown in the inset of Fig. 13(a). This effect is visible in RRB as shown in Fig. 5(b) of Ref. 24. Here it is shown that for the nonrotating case, $\lambda_u<\lambda_\theta^{sl}$ when $\mathrm{Pr}\lesssim 1$. When the rotation rate is increased, i.e., Ro is lowered, this transition shifts toward higher Pr and for $\mathrm{Ro}=0.1$ $\lambda_u<\lambda_\theta^{sl}$ when $\mathrm{Pr}\lesssim 9$.

In summary, the laminar rotating BL theory explains the $\mathrm{Ro}^{1/2}$ scaling of the kinetic BL thickness in RRB convection and the shift of the position, where $\lambda_u=\lambda_\theta$ toward higher Pr when the flow is dominated by rotational effects.

IV. MODEL FOR SMOOTH ONSET IN RRB CONVECTION

In this section, we will introduce a model in the spirit of the GL approach in order to describe the smooth increase in the heat transfer as a function of Ro that is observed for relatively low Ra and weak background rotation. Since the GL theory assumes smooth transitions between different turbulent states, the model is limited to the relatively low Ra number regime, since a sharp onset as function of Ro is found for $\mathrm{Ra}\gtrsim 1\times 10^8$. Furthermore, we assume that then the LSC, a basic ingredient of the GL model, is still present. In this simple model, we neglect the influence of Ekman pumping because it is a local effect that is rather insignificant at weak background rotation. This is supported by the results in Fig. 6 and the supplementary material of Ref. 18, where we find no evidence for Ekman pumping at weak background rotation. When strong rotation is applied, Ekman pumping is the dominant effect and the validity regime of our model is thus restricted to weak background rotation. The basic idea of the model is to combine the effect of the LSC roll, which is implemented in the GL theory by the use of the laminar Prandtl–Blasius theory over an infinitely large plate and the influence of rotation on the thermal BL.

Applying laminar BL theory requires that the viscous BL above the flat rotating plate does not break down. This assumption will now be verified. The stability for the von Kármán flow has been studied theoretically and experimentally by Lingwood,[48–50] showing that instability occurs at $\mathrm{Re}\approx 510$, where Re is defined as $\mathrm{Re}=r\sqrt{\Omega/\nu}$ (with r the distance to the rotation axis). Lingwood also pointed out that other experimental studies show the same transition point within a very narrow Reynolds number range $\mathrm{Re}=513\pm 15$ (see Ref. 48 and references therein). More recent experiments show similar results.[51,52] For the Ekman case, the instability occurs at $\mathrm{Re}\approx 200$ (see Ref. 50). For the case under consideration it can be shown that $\mathrm{Re}\lesssim 55$ (with $r=12.5$ cm, $\Omega\approx 0.20$ rad/s, and $\nu=1\times 10^6$ m^2/s).[17] It can safely be conjectured that laminar BL theory can be applied as the estimated Reynolds number is an order of magnitude smaller than the critical Reynolds number. For further discussion on the stability of the rotational flow, we refer to the classic Refs. 8 and 53.

We introduce $\lambda_{\theta R}=\bar{\lambda}_\theta^{sl}(\mathrm{Pr})\sqrt{\nu/\Omega}$ [see $\bar{\lambda}_\theta^{sl}(\mathrm{Pr})$ in Fig. 13(a)] as the thermal BL thickness based on the background rotation and $\lambda_{\theta C}$ as the BL thickness based on the LSC roll. Furthermore, Γ is the diameter-to-height aspect ratio of the RB cell and we set the radial length $r=(\Gamma L)/2$. Note that this is analogous to the length L which is introduced in the GL theory for the length of the plate. Thus the Reynolds number based on the background rotation is

$$\mathrm{Re}_R=\frac{\Omega L^2\Gamma^2}{4\nu}\propto\frac{1}{\mathrm{Ro}}. \tag{20}$$

To calculate $\lambda_{\theta R}$ we used $\nu=1\times 10^{-6}$ m^2/s (water) and $\Gamma=1$ and we set $\lambda_{\theta R}=\lambda_{\theta C}$ at $\mathrm{Ro}=\infty$. The strength of the LSC roll is taken constant and $\lambda_{\theta C}$ is known from $\lambda_{\theta C}/L=(2\mathrm{Nu})^{-1}$.

We model the increase of Nu as a crossover between a convection role dominated BL and a rotation dominated BL. Thus, without rotation, the BL thickness is determined by the LSC roll, i.e., $\lambda_\theta=\lambda_{\theta C}$, and when rotation becomes dominant, the BL thickness is determined by the rotating BL thickness, i.e., $\lambda_\theta=\lambda_{\theta R}$. We now model the crossover between these two limiting cases as

$$\frac{\lambda_\theta}{L}=\frac{\sqrt{\mathrm{Re}_R}\lambda_{\theta R}+\alpha^*\sqrt{\mathrm{Re}_C}\lambda_{\theta C}}{(\sqrt{\mathrm{Re}_R}+\alpha^*\sqrt{\mathrm{Re}_C})L}. \tag{21}$$

Here, the square root of Reynolds has been chosen since the dimensionless BL thicknesses scale with $1/\sqrt{\mathrm{Re}}$. We rewrite the above equation in terms of Ro, using $\mathrm{Re}_R\propto\mathrm{Re}_C/\mathrm{Ro}$,

$$\frac{\lambda_\theta}{L}=\frac{\frac{1}{\alpha\sqrt{\mathrm{Ro}}}\lambda_{\theta R}+\lambda_{\theta_C}}{\left(\frac{1}{\alpha\sqrt{\mathrm{Ro}}}+1\right)L} \tag{22}$$

and we use the free parameter α to fit the model with the numerical data shown in Fig. 5. It can be concluded that the presented model, based on the approach of the GL theory, indeed reflects the increase of Nu (as compared to the case without rotation) observed at relatively low Ra number ($\mathrm{Ra}=4\times10^7$) when the LSC is still present. Furthermore, the thickness of the thermal BLs is also reflected correctly by the model. Note that the large value of the parameter $\alpha=55$ indicates that the influence of the rotation is rather weak before Ekman pumping sets in and it also explains that for higher Ra ($\mathrm{Ra}\gtrsim1\times10^8$), no heat transfer enhancement is observed below onset. The sudden (instead of smooth) transition is then fully determined by the rotation rate where Ekman pumping sets in. This may be because at higher Ra, the thermal BL is already much thinner due to the stronger LSC and therefore the effect of weak rotation is not sufficient to result in a significant thinner thermal BL. When $\mathrm{Ro}<\mathrm{Ro}_c$, the model cannot be used, since Ekman pumping is dominant in this regime which is responsible for the strong increase observed in Nu when $\mathrm{Ro}<\mathrm{Ro}_c$.

V. CONCLUSIONS

To summarize, we have studied the effect of rotation on the RB system at relatively low Ra number, i.e., $\mathrm{Ra}=4\times10^7$ by using DNS. We find a smooth increase of the heat transfer as function of the rotation rate when weak rotation is applied. To describe this heat transfer enhancement, we have extended the GL theory to the rotating case by studying the influence of rotation on the scaling of the thermal BL thickness. It is based on a similar approach as in the laminar Prandtl–Blasius BL theory over an infinitely large plate, as we analyzed the flow over an infinitely large rotating disk where the fluid at infinity is allowed to rotate. Just as in the Prandtl–Blasius BL theory, we used a passive temperature field to calculate the characteristics of the thermal BL. It turns out that weak background rotation does not influence the scaling of the BL thickness in the high Pr regime because again, $\mathrm{Pr}^{-1/3}$ scaling is found. However, rotation does influence the scaling in the low Pr regime where we find a scaling of Pr^{-1} instead of $\mathrm{Pr}^{-1/2}$ found in the Prandtl–Blasius BL theory. With our model for the thermal BL thickness [see Eq. (22)], we can explain the increased heat transfer observed in the relatively low Ra number regime before the strength of the LSC decreases. The model neglects the effect of Ekman pumping as this effect is rather insignificant before the strength of the LSC decreases, i.e., the regime to which the model is applied. This means that the model cannot predict the heat transfer enhancement that is observed at moderate rotation rates where Ekman pumping is the dominant mechanism. The contrast between the smooth onset at $\mathrm{Ra}=4\times10^7$ and the sharp onset at $\mathrm{Ra}\gtrsim1\times10^8$ is remarkable since only a small shift in the Ra-Pr-Ro phase space is involved.

ACKNOWLEDGMENTS

We thank R. Verzicco for providing us with the numerical code and F. Fontenele Araujo, F. Busse, G. J. F. van Heijst, C. Sun, and L. van Wijngaarden for discussions. The work is sponsored by the Foundation for Fundamental Research on Matter (FOM) and the National Computing Facilities (NCF), both sponsored by NWO. The numerical calculations have been performed on the Huygens cluster of SARA in Amsterdam.

APPENDIX: EKMAN BOUNDARY LAYER THEORY

In this appendix, the results obtained from the model with weak background rotation will be compared with analytic results obtained from Ekman BL theory,[54] which uses a rotating reference frame. In the Ekman case, the fluid at infinity is rotating at almost the same velocity as the disk, i.e., the limiting case of the model will be checked. We will indicate all quantities calculated in the rotating reference frame with an asterisk.

We will use the BEK (Bödewadt–Ekman–von Kármán) model, presented in Refs. 50, 55, and 56 to derive a similar ODE as in Sec. III for the temperature advection equation in the rotating reference frame. In the BEK model, the following self-similarity assumption for the axial velocity is proposed:

$$w=\sqrt{\nu\Omega^*}\mathrm{Ro}^*H^*(\xi), \tag{A1}$$

where $\xi=z\sqrt{\Omega^*/\nu}$. Here, Ω^* is a system rotation rate, and Ro^* is a constant determined by the rotation rate. We call this still the Rossby number since it also represents a dimensionless inverse rotation. In the BEK model, Ro^*, $\Delta\Omega$, and Ω^*, respectively, are defined as

$$\mathrm{Ro}^*=\frac{\Delta\Omega}{\Omega^*}, \tag{A2}$$

$$\Delta\Omega=\Omega_F-\Omega_D, \tag{A3}$$

$$\Omega^*=\frac{\Omega_F}{2-\mathrm{Ro}^*}+\frac{\Omega_D}{2+\mathrm{Ro}^*}. \tag{A4}$$

We obtain the following temperature advection equation in the BEK model:

$$\tilde{\theta}' = \mathrm{Pr}H^*(\xi)\mathrm{Ro}^*\tilde{\theta}'. \tag{A5}$$

From Eqs. (A2)–(A4) one obtains, after some algebra,

$$s = \frac{\Omega_F}{\Omega_D} = \left[\frac{2+\mathrm{Ro}^*-\mathrm{Ro}^{*2}}{2-\mathrm{Ro}^*-\mathrm{Ro}^{*2}}\right]. \tag{A6}$$

This means for the Ekman case ($s \approx 1$, i.e., $\mathrm{Ro}^* \to 0$) that $\Omega_F \simeq \Omega_D(1+\mathrm{Ro}^*)$. Thus, when the fluid at infinity is rotating slower than the disk, Ro^* is negative. From now on we assume Ro^* to be negative, i.e., $s<1$.

Using Ekman BL theory,[54] one can derive analytic solutions for the radial and tangential velocity profiles in the rotating reference frame. These analytical solutions read[54]

$$u_E = -\Delta\Omega r e^{-\zeta}\sin\zeta = r\Omega^*\mathrm{Ro}^*F^*(\zeta), \tag{A7}$$

$$v_E = \Delta\Omega r(1-e^{-\zeta}\cos\zeta) = r\Omega^*\mathrm{Ro}^*G^*(\zeta), \tag{A8}$$

with ζ as in Eq. (3). With the analytic expression for the radial velocity (A7) and the continuity equation, one obtains

$$w_E = \Delta\Omega\sqrt{\frac{\nu}{\Omega_D}}(1-e^{-\zeta}[\sin\zeta+\cos\zeta]) = \sqrt{\nu\Omega^*}\mathrm{Ro}^*H^*(\zeta). \tag{A9}$$

In the case $\mathrm{Ro}^* \to 0$, it is found that $\Omega_D \approx \Omega^*$, thus $\xi \approx \zeta$. In particular, the expression for the axial flow reduces to $H^*(\xi) = \sqrt{\Omega^*/\Omega_D}(1-e^{-\xi}[\sin\xi+\cos\xi])$, where $\sqrt{\Omega^*/\Omega_D} \approx 1$. We find that the analytic expressions and the above numerical solutions are identical within numerical accuracy for the limiting case (Ekman solution, $s \approx 1$, $\mathrm{Ro}^* \to 0$). (Note that a coordinate transformation has to be applied as the Ekman solution is expressed in the corotating reference frame, whereas the numerical solution has been defined in the laboratory frame.)

Now we use this approach to calculate the BL characteristics for the Ekman layer. With the temperature advection equation (A5) and the analytic expression $H^*(\xi)$ for the axial velocity, we determine the effective scaling exponent γ in $\bar{\lambda}_\theta \sim \mathrm{Pr}^\gamma$ as function of Pr for $\mathrm{Ro}^* = -10^{-3}$ and $\mathrm{Ro}^* = -10^{-5}$. Figure 13 shows that when Ro^* goes to zero, the low Pr regime ($\bar{\lambda}_\theta \gg \bar{\lambda}_u$) is extended to higher Pr because the kinetic BL thickness becomes thinner and the axial velocity becomes smaller, i.e., the thermal BL becomes thicker.

Substitution of $H^*(\xi)$ in Eq. (A5) yields the following expression for the temperature gradient in the Ekman layer:

$$\frac{d\tilde{\theta}}{d\xi} = C_1 e^{[(e^{-\xi}\cos\xi+\xi)\mathrm{PrRo}^*]}, \tag{A10}$$

where C_1 is a constant of integration which does not depend on ξ. To determine the constant C_1, and thereby Nu, one needs to integrate Eq. (A10). An analytic result can be derived by substituting $\cos\xi = (e^{i\xi}+e^{-i\xi})/2$, $A = \mathrm{PrRo}^*$, $z = A\xi$, $B = (i-1)/A$ (and $\bar{B}$ the complex conjugate of B), and evaluate the integral

$$\tilde{\theta}(z) = \frac{C_1}{A}\int e^z e^{1/2Ae^{Bz}} e^{1/2Ae^{\bar{B}z}} dz + C_2. \tag{A11}$$

The integration constants C_1 and C_2 are determined by the boundary conditions $\tilde{\theta}(\xi=0)=1$ and $\tilde{\theta}(\xi\to\infty)=0$: $C_2=0$ and, for small A,

$$\frac{1}{C_1} \approx \frac{1}{A} - \frac{1}{2}A - \frac{3}{16}A^2 + \mathcal{O}(A^3). \tag{A12}$$

The thermal BL thickness scales according to $\bar{\lambda}_\theta \propto e^{-A}/C_1$. With Eq. (A12), we immediately see that in the small Prandtl number limit: $\bar{\lambda}_\theta \propto \mathrm{Pr}^{-1}$. Comparison with Fig. 13(b) reveals that the analytic results are in good agreement with the numerical data for $\bar{\lambda}_\theta$ represented by the solid lines. Moreover, it predicts the scaling for $\mathrm{Ro}^* = -1$ (the von Kármán case, thus far outside the regime of applicability of the Ekman analysis) surprisingly well [see Fig. 13(b)].

[1] G. Ahlers, S. Grossmann, and D. Lohse, "Heat transfer and large scale dynamics in turbulent Rayleigh–Bénard convection," Rev. Mod. Phys. **81**, 503 (2009).
[2] G. Ahlers, "Turbulent convection," Phys. **2**, 74 (2009).
[3] D. Lohse and K. Q. Xia, "Small-scale properties of turbulent Rayleigh–Bénard convection," Annu. Rev. Fluid Mech. **42**, 335 (2010).
[4] S. Grossmann and D. Lohse, "Scaling in thermal convection: A unifying view," J. Fluid Mech. **407**, 27 (2000).
[5] S. Grossmann and D. Lohse, "Thermal convection for large Prandtl number," Phys. Rev. Lett. **86**, 3316 (2001).
[6] S. Grossmann and D. Lohse, "Prandtl and Rayleigh number dependence of the Reynolds number in turbulent thermal convection," Phys. Rev. E **66**, 016305 (2002).
[7] S. Grossmann and D. Lohse, "Fluctuations in turbulent Rayleigh–Bénard convection: The role of plumes," Phys. Fluids **16**, 4462 (2004).
[8] S. Chandrasekhar, *Hydrodynamic and Hydromagnetic Stability* (Dover, New York, 1981).
[9] Y. Liu and R. E. Ecke, "Heat transport scaling in turbulent Rayleigh–Bénard convection: Effects of rotation and Prandtl number," Phys. Rev. Lett. **79**, 2257 (1997).
[10] Y. Liu and R. E. Ecke, "Heat transport measurements in turbulent rotating Rayleigh–Bénard convection," Phys. Rev. E **80**, 036314 (2009).
[11] H. T. Rossby, "A study of Bénard convection with and without rotation," J. Fluid Mech. **36**, 309 (1969).
[12] J. M. Pfotenhauer, P. G. J. Lucas, and R. J. Donnelly, "Stability and heat transfer of rotating cryogens. Part 2. Effects of rotation on heat-transfer properties of convection in liquid He," J. Fluid Mech. **145**, 239 (1984).
[13] B. M. Boubnov and G. S. Golitsyn, "Experimental study of convective structures in rotating fluids," J. Fluid Mech. **167**, 503 (1986).
[14] B. M. Boubnov and G. S. Golitsyn, "Temperature and velocity field regimes of convective motions in a rotating plane fluid layer," J. Fluid Mech. **219**, 215 (1990).
[15] F. Zhong, R. E. Ecke, and V. Steinberg, "Rotating Rayleigh–Bénard convection: Asymmetric modes and vortex states," J. Fluid Mech. **249**, 135 (1993).
[16] E. M. King, S. Stellmach, J. Noir, U. Hansen, and J. M. Aurnou, "Boundary layer control of rotating convection systems," Nature (London) **457**, 301 (2009).
[17] J.-Q. Zhong, R. J. A. M. Stevens, H. J. H. Clercx, R. Verzicco, D. Lohse, and G. Ahlers, "Prandtl-, Rayleigh-, and Rossby-number dependence of heat transport in turbulent rotating Rayleigh–Bénard convection," Phys. Rev. Lett. **102**, 044502 (2009).
[18] R. J. A. M. Stevens, J.-Q. Zhong, H. J. H. Clercx, G. Ahlers, and D. Lohse, "Transitions between turbulent states in rotating Rayleigh–Bénard convection," Phys. Rev. Lett. **103**, 024503 (2009).
[19] P. Oresta, G. Stingano, and R. Verzicco, "Transitional regimes and rotation effects in Rayleigh–Bénard convection in a slender cylindrical cell," Eur. J. Mech. B/Fluids **26**, 1 (2007).
[20] K. Julien, S. Legg, J. McWilliams, and J. Werne, "Rapidly rotating Rayleigh–Bénard convection," J. Fluid Mech. **322**, 243 (1996).
[21] M. Sprague, K. Julien, E. Knobloch, and J. Werne, "Numerical simulation of an asymptotically reduced system for rotationally constrained convection," J. Fluid Mech. **551**, 141 (2006).

[22]R. P. J. Kunnen, H. J. H. Clercx, and B. J. Geurts, "Breakdown of large-scale circulation in turbulent rotating convection," Europhys. Lett. **84**, 24001 (2008).
[23]S. Schmitz and A. Tilgner, "Heat transport in rotating convection without Ekman layers," Phys. Rev. E **80**, 015305 (2009).
[24]R. J. A. M. Stevens, H. J. H. Clercx, and D. Lohse, "Optimal Prandtl number for heat transfer in rotating Rayleigh–Bénard convection," New J. Phys. **12**, 075005 (2010).
[25]P. Vorobieff and R. E. Ecke, "Vortex structure in rotating Rayleigh–Bénard convection," Physica D **123**, 153 (1998).
[26]P. Vorobieff and R. E. Ecke, "Turbulent rotating convection: An experimental study," J. Fluid Mech. **458**, 191 (2002).
[27]J. Niemela, S. Babuin, and K. Sreenivasan, "Turbulent rotating convection at high Rayleigh and Taylor numbers," J. Fluid Mech. **649**, 509 (2010).
[28]R. P. J. Kunnen, H. J. H. Clercx, and B. J. Geurts, "Heat flux intensification by vortical flow localization in rotating convection," Phys. Rev. E **74**, 056306 (2006).
[29]R. Verzicco and P. Orlandi, "A finite-difference scheme for three-dimensional incompressible flow in cylindrical coordinates," J. Comput. Phys. **123**, 402 (1996).
[30]R. Verzicco and R. Camussi, "Prandtl number effects in convective turbulence," J. Fluid Mech. **383**, 55 (1999).
[31]R. Verzicco and R. Camussi, "Numerical experiments on strongly turbulent thermal convection in a slender cylindrical cell," J. Fluid Mech. **477**, 19 (2003).
[32]R. J. A. M. Stevens, R. Verzicco, and D. Lohse, "Radial boundary layer structure and Nusselt number in Rayleigh–Bénard convection," J. Fluid Mech. **643**, 495 (2010).
[33]R. Kunnen, B. Geurts, and H. Clercx, "Turbulence statistics and energy budget in rotating Rayleigh–Bénard convection," Eur. J. Mech. B/Fluids **28**, 578 (2009).
[34]R. P. J. Kunnen, B. J. Geurts, and H. J. H. Clercx, "Experimental and numerical investigation of turbulent convection in a rotating cylinder," J. Fluid Mech. **642**, 445 (2010).
[35]O. Shishkina, R. J. A. M. Stevens, S. Grossmann, and D. Lohse, "Boundary layer structure in turbulent thermal convection and its consequences for the required numerical resolution," New J. Phys. **12**, 075022 (2010).
[36]S. Lam, X. D. Shang, S. Q. Zhou, and K.-Q. Xia, "Prandtl-number dependence of the viscous boundary layer and the Reynolds-number in Rayleigh–Bénard convection," Phys. Rev. E **65**, 066306 (2002).
[37]C. Sun, Y. H. Cheung, and K. Q. Xia, "Experimental studies of the viscous boundary layer properties in turbulent Rayleigh–Bénard convection," J. Fluid Mech. **605**, 79 (2008).
[38]Q. Zhou and K.-Q. Xia, "Measured instantaneous viscous boundary layer in turbulent Rayleigh–Bénard convection," Phys. Rev. Lett. **104**, 104301 (2010).
[39]H. Schlichting, *Boundary Layer Theory*, 7th ed. (McGraw-Hill, New York, 1979).
[40]L. G. Loitsianski and W. Szablewski, *Laminare Grenzschichten*, 2nd ed. (Akademie-Verlag, Berlin, 1967).
[41]M. H. Rogers and G. Lance, "The rotationally symmetric flow of a viscous fluid in the presence of an infinite rotating disk," J. Fluid Mech. **7**, 617 (1960).
[42]L. van Wijngaarden, "On multiple solutions and other phenomena in rotating fluids," Fluid Dyn. Trans. **12**, 157 (1985).
[43]P. J. Zandbergen and D. Dijkstra, "Non-unique solutions of the Navier–Stokes equations for the Kármán swirling flow," J. Eng. Math. **11**, 167 (1977).
[44]L. D. Landau and E. M. Lifshitz, *Fluid Mechanics* (Pergamon, Oxford, 1987).
[45]E. M. Sparrow and J. L. Gregg, "Heat transfer from a rotating disk to fluids of any Prandtl number," ASME Trans. J. Heat Transfer **81**, 249 (1959).
[46]N. R. Vira and D. N. Fan, "Temperature distribution in generalized von Karman rotating flows," Numer. Heat Transfer **3**, 483 (1980).
[47]K. Millsaps and K. Pohlhausen, "Heat transfer by laminar flow from a rotating plate," J. Aeronaut. Sci. **19**, 120 (1952).
[48]R. J. Lingwood, "Absolute instability of the boundary layer on a rotating disk," J. Fluid Mech. **299**, 17 (1995).
[49]R. J. Lingwood, "An experimental study of absolute instabilities of the rotating-disk boundary-layer flow," J. Fluid Mech. **314**, 373 (1996).
[50]R. J. Lingwood, "Absolute instability of the Ekman layer and the related rotating flows," J. Fluid Mech. **331**, 405 (1997).
[51]A. J. Colley, P. J. Thomas, P. W. Carpenter, and A. J. Cooper, "An experimental study of boundary-layer transition over a rotating compliant disk," Phys. Fluids **11**, 3340 (1999).
[52]F. Zoueshtiagh, R. Ali, A. J. Colley, P. J. Thomas, and P. W. Carpenter, "Laminar-turbulent boundary-layer transition over a rough rotating plate," Phys. Fluids **15**, 2441 (2003).
[53]F. H. Busse, "Thermal instabilities in rapidly rotating flows," J. Fluid Mech. **44**, 441 (1970).
[54]H. P. Greenspan, *The Theory of Rotating Flows* (Breukelen, Brookline, 1990).
[55]A. J. Faller, "Instability and transition of disturbed flow over a rotating disk," J. Fluid Mech. **230**, 245 (1991).
[56]H. A. Jasmine and J. S. B. Gajjar, "Absolute instability of the von Kármán, Bödewadt and Ekman flows between a rotating disc and a stationary lid," Philos. Trans. R. Soc. London, Ser. A **363**, 1131 (2005).